# Perovskite–organic tandem solar cells with indium oxide interconnect

https://doi.org/10.1038/s41586-022-04455-0

Received: 9 December 2020

Accepted: 24 January 2022

K. O. Brinkmann[1,2,10]✉, T. Becker[1,2,10], F. Zimmermann[1,2], C. Kreusel[1,2], T. Gahlmann[1,2], M. Theisen[1,2], T. Haeger[1,2], S. Olthof[3], C. Tückmantel[1,2], M. Günster[1,2], T. Maschwitz[1,2], F. Göbelsmann[1,2], C. Koch[3], D. Hertel[3], P. Caprioglio[4,5], F. Peña-Camargo[4], L. Perdigón-Toro[4], A. Al-Ashouri[6], L. Merten[8], A. Hinderhofer[8], L. Gomell[9], S. Zhang[9], F. Schreiber[8], S. Albrecht[6,7], K. Meerholz[3], D. Neher[4], M. Stolterfoht[4] & T. Riedl[1,2]✉

Multijunction solar cells can overcome the fundamental efficiency limits of single-junction devices. The bandgap tunability of metal halide perovskite solar cells renders them attractive for multijunction architectures[1]. Combinations with silicon and copper indium gallium selenide (CIGS), as well as all-perovskite tandem cells, have been reported[2–5]. Meanwhile, narrow-gap non-fullerene acceptors have unlocked skyrocketing efficiencies for organic solar cells[6,7]. Organic and perovskite semiconductors are an attractive combination, sharing similar processing technologies. Currently, perovskite–organic tandems show subpar efficiencies and are limited by the low open-circuit voltage ($V_{oc}$) of wide-gap perovskite cells[8] and losses introduced by the interconnect between the subcells[9,10]. Here we demonstrate perovskite–organic tandem cells with an efficiency of 24.0 per cent (certified 23.1 per cent) and a high $V_{oc}$ of 2.15 volts. Optimized charge extraction layers afford perovskite subcells with an outstanding combination of high $V_{oc}$ and fill factor. The organic subcells provide a high external quantum efficiency in the near-infrared and, in contrast to paradigmatic concerns about limited photostability of non-fullerene cells[11], show an outstanding operational stability if excitons are predominantly generated on the non-fullerene acceptor, which is the case in our tandems.
The subcells are connected by an ultrathin (approximately 1.5 nanometres) metal-like indium oxide layer with unprecedented low optical/electrical losses. This work sets a milestone for perovskite–organic tandems, which outperform the best p–i–n perovskite single junctions[12] and are on a par with perovskite–CIGS and all-perovskite multijunctions[13].

In general, multijunction solar cells are designed as a series connection of wide bandgap and narrow bandgap subcells with complementary absorption spectra. An improved overlap with the solar spectrum and reduced thermalization losses are the keys to overcoming the Shockley–Queisser efficiency limit of single junctions[14].

Hybrid metal halide perovskites have received tremendous attention as photoactive materials in solar cells[15]. Their typical $ABX_3$ composition consists of methylammonium ($MA^+$), formamidinium ($FA^+$) or $Cs^+$ ions on the A site, $Pb^{2+}$ ions on the B site and halide ions, such as $I^-$ or $Br^-$, on the X site. Some members of this family, for example, $FA_xCs_{1-x}Pb(I_yBr_{1-y})_3$, afford tunability of the bandgap energy ($E_g$) between 1.5 and 2.3 eV, mainly by variation of the I:Br ratio[16,17].

All-perovskite tandem cells require narrow-gap materials ($E_g < 1.3$ eV), where the lead is partially replaced by tin[18,19]. However, severe stability issues are linked to the unwanted transformation of $Sn^{2+}$ to $Sn^{4+}$, which leads to non-intentional p-type doping and an overall degradation of device performance. This effect can be slowed down to some extent by additives, such as a surplus of sacrificial Sn(0) inside the active layer[4]. Alternatively, c-Si or copper indium gallium selenide back-cells have been used[2,3] in combination with a wide-gap perovskite front-cell. Some of these tandems already outperform the best c-Si single junctions[2,20]. On the downside, perovskite/c-Si tandems are not compatible with low-temperature, low-cost, large-area manufacturing—a vision that is frequently quoted for perovskite solar technology. In this regard, organic solar cells (OSCs) represent an attractive option as narrow-gap back-cells. OSCs were typically based on so-called bulk-heterojunction architectures, which were formed by a blend of a donor polymer and a fullerene derivative as acceptor[21]. Owing to the limited tunability of the energy levels of the fullerene, progress in OSCs came to a halt at efficiency levels of about 11% (ref. [22]). However, with the recent introduction

---

[1]Institute of Electronic Devices, University of Wuppertal, Wuppertal, Germany. [2]Wuppertal Center for Smart Materials & Systems, University of Wuppertal, Wuppertal, Germany. [3]Department of Chemistry, University of Cologne, Cologne, Germany. [4]Soft Matter Physics and Optoelectronics, University of Potsdam, Potsdam, Germany. [5]Department of Physics, University of Oxford, Clarendon Laboratory, Oxford, UK. [6]Young Investigator Group - Perovskite Tandem Solar Cells, Helmholtz-Zentrum Berlin, Berlin, Germany. [7]Faculty of Electrical Engineering and Computer Science, Technical University Berlin, Berlin, Germany. [8]Institute of Applied Physics, University of Tübingen, Tübingen, Germany. [9]Max-Planck-Institut für Eisenforschung GmbH, Düsseldorf, Germany. [10]These authors contributed equally: K. O. Brinkmann, T. Becker. ✉e-mail: brinkmann@uni-wuppertal.de; t.riedl@uni-wuppertal.de

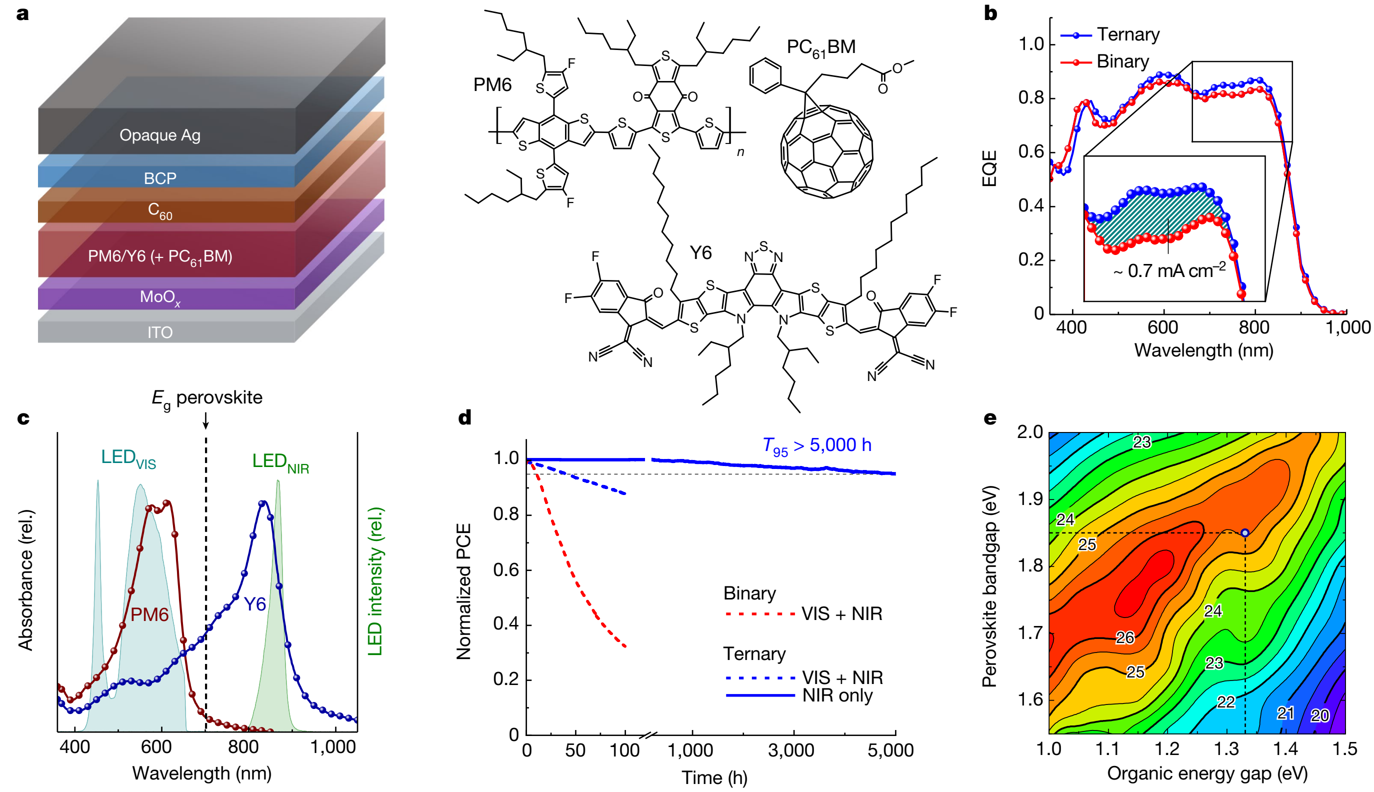

**Fig. 1 | Architecture and properties of the organic subcell. a**, Layer sequence of the single-junction OSC and chemical structure of the molecules used in the photoactive layer. **b**, EQE of binary (PM6:Y6) and ternary (PM6:Y6:PC$_{61}$BM) cells with a magnified view of the spectral region >650 nm, which is the relevant range of operation for the OSC in a perovskite–organic tandem cell. **c**, Absorption spectra of the donor and acceptor molecules used in the photoactive layer. The vertical line marks the $E_g$ of a possible wide-gap front-cell material. Spectra of (filtered) LEDs used in the stability assessment to selectively excite the donor/acceptor are also shown (LED$_{VIS}$ and LED$_{NIR}$); rel., relative. **d**, Normalized PCE showing the long-term stability of binary and ternary organic cells continuously operated using LED light sources with emission spectra shown in **c** (one-sun-equivalent, nitrogen atmosphere, 25 °C) in the MPP with exciton generation on both acceptor and donor (VIS + NIR) or only on the acceptor (NIR). Note the break in the *x* axis. $T_{95}$ denotes the time after which the initial PCE has dropped to 95% of its initial value. **e**, Semi-empirical model of the tandem cell efficiency versus the energy gap of organic and perovskite subcells. The intersection of the dashed lines corresponds to the energy gap of the PM6:Y6:PC$_{61}$BM back-cell and the matching energy gap of the perovskite front-cell. This simulation states a conservative scenario assuming open-circuit voltage loss ($\Delta V_{oc}$) of 0.5 V and a FF of 80%. A more optimistic (yet still realistic) model ($\Delta V_{oc}$ = 0.4 V, FF = 85%) yields a maximum efficiency higher than 31% (Supplementary Fig. 8).

of non-fullerene acceptors (NFAs), OSCs started to see a second wave of outstanding advancement, which has propelled their efficiencies beyond 18% (refs. [6,7,23]). This progress mainly draws from the narrow energy gap of the acceptor moiety and an efficient exciton dissociation that requires only small energy offsets between donor and acceptor, which is the key to unlocking low losses in $V_{oc}$ compared to $E_g/q$, where $q$ is the elementary charge, while still providing a high external quantum efficiency (EQE) and thus high short-circuit current densities ($J_{sc}$)[24,25].

## Narrow-gap organic subcell

For the narrow-gap subcell in our tandem architecture, we consider an organic photoactive system based on the polymer PM6, which contains a fluorinated thienyl benzodithiophene, and the NFA Y6, which consists of a ladder-type dithienothiophen[3.2-*b*]-pyrrolobenzothiadiazole central moiety and 2-(5,6-difluoro-3-oxo-2,3-dihydro-1*H*-inden-1-ylidene) malononitrile units (Fig. 1a)[26]. We use a p–i–n-type device architecture with molybdenum oxide (MoO$_x$) as the hole extraction layer (HEL) and a bilayer of C$_{60}$/2,9-dimethyl-4,7-diphenyl-1,10-phenanthroline (BCP) for efficient electron extraction. Our cells with binary PM6:Y6 blends (1:1.2) provide a power conversion efficiency (PCE) of up to 16.5%. The EQE spectrum of these devices extends beyond 900 nm (Fig. 1b and Supplementary Fig. 1). Adding a certain concentration of the fullerene derivative [6,6]-phenyl-C$_{61}$-butyric acid methyl ester (PC$_{61}$BM) into the PM6:Y6 photoactive layer to form a so-called ternary system, that is, PM6:Y6:PC$_{61}$BM (1:1.2:0.2), improves the blend morphology, which results in enhanced charge transport and reduced non-radiative recombination[27,28]. Thus, a notable boost in cell characteristics is achieved with a PCE up to 17.5% (Table 1; for device statistics see Supplementary Fig. 2). We want to highlight a notably enhanced EQE of >85% for the ternary cells in the range of $\lambda > 650$ nm, which is the spectral region of operation when combined with a wide-gap front-cell in a tandem solar cell. The absorption spectra of PM6 and Y6 (Fig. 1c) show that, for $\lambda > 650$ nm, excitons are predominantly generated on the Y6, which will be shown to be the key that unlocks outstanding device stability.

Stability of NFA cells under continuous operation is still a serious concern and a subject of vigorous scientific research[29]. To assess the stability of our binary and ternary cells under the illumination conditions applicable in a prospective perovskite–organic tandem cell, we used a filtered white light-emitting diode (LED) (labelled as LED$_{VIS}$) and a near-infrared (NIR) LED (peak at 850 nm; labelled as LED$_{NIR}$) as light sources, which predominantly create excitons on the PM6 or Y6, respectively (Fig. 1c). Under combined visible/NIR illumination (details in Methods), binary and ternary cells show a notable decay of the PCE after continuous operation in the maximum power point (MPP) (Fig. 1d), mainly due to a loss in fill factor (FF) (Supplementary Fig. 3). This degradation motif has previously been explained by a photo-induced reorganization in the donor/acceptor blend and the formation of microscopic aggregates of NFA molecules, which

**Table 1 | Champion solar cell characteristics**

| | Scan direction | PCE (%) | FF (%) | $V_{oc}$ (V) | $J_{sc}$ (mA cm$^{-2}$) |
|---|---|---|---|---|---|
| PSC | Reverse | 16.8 | 81 | 1.34 | 15.6 |
| | Forward | 16.4 | 80 | 1.33 | 15.5 |
| OSC | Invariant | 17.5 | 75 | 0.87 | 26.7 |
| Tandem | Reverse | 24.0 | 80 | 2.15 | 14.0 |
| | Forward | 23.8 | 79 | 2.14 | 14.1 |

The PCE, FF, open-circuit voltage ($V_{oc}$) and short-circuit current ($J_{sc}$) of the OSC and PSC single junctions and the tandem cell derived from their respective *J*–*V* characteristics. Note, for all cells, the $J_{sc}$ agrees with the current density obtained from the EQE spectra (deviation less than 1%).

leads to a reduced electron mobility and enhanced recombination[30]. Owing to their improved blend morphology, the decay of the ternary cells is notably slower than that of the binary cells[29]. However, most strikingly, under NIR illumination, where excitons are solely generated on the Y6, the devices did not show any burn-in, and we found only minimal signs of degradation even under long-term continuous operation for more than 5,000 h (retaining 95% of the original efficiency). These findings indicate that the detrimental morphological changes discussed above would require excitation of the donor polymer PM6 and that they can be substantially mitigated if it is predominantly the Y6 NFA that is excited. Atomic force microscopy (AFM) and grazing incidence wide-angle X-ray scattering (GIWAXS) did not show morphological changes on continuous illumination with $LED_{VIS}$ + $LED_{NIR}$ under inert conditions, and the results of grazing incidence small-angle X-ray scattering (GISAXS) indicate only some minor morphological changes at the surface of samples after ageing (Supplementary Figs. 4–6). On the other hand, we found that on continuous illumination with the white LED under inert conditions the photoluminescence quantum yield of PM6 shows a notable degradation, whereas the Y6 is less affected (Supplementary Fig. 7). Therefore, photo-induced degradation of PM6 could likewise play a substantial role, in addition to possible morphological changes. In any event, our findings contradict the paradigmatic association of non-fullerene solar cells with operational instability, and they present the encouraging prospect that the long-term operational stability of perovskite–organic tandem cells will not be limited by the narrow-gap OSCs. This is in marked contrast to all-perovskite tandems, where the instability of Sn-based narrow-gap perovskite solar cells (PSCs) is still a very serious issue.

The PM6:Y6 organic system provides an energy gap of 1.33 eV (ref. [26]), and we conducted a semi-empirical electro-optical simulation to identify a suitable wide-gap PSC for a tandem cell. Details of the simulation can be found in the Supplementary Information. According to Fig. 1e, an efficiency of 25.5% is predicted with a perovskite bandgap in the range of 1.85–1.92 eV, assuming a tandem FF of 80% and a loss in $V_{oc}$ compared to $E_g/q$ of 0.5 V, in each subcell. In a more optimistic scenario (FF = 85% and loss in $V_{oc}$ compared to $E_g/q$ of 0.4 V), a tandem of a narrow-gap OSC ($E_g$ = 1.15 eV) with a wide-gap PSC ($E_g$ = 1.75 eV), provides the prospect of reaching an efficiency of 31.3% (Supplementary Fig. 8). So far, efficient OSCs with $E_g$ = 1.15 eV have not been developed.

## Wide-gap perovskite subcell

We selected $FA_{0.8}Cs_{0.2}Pb(I_{0.5}Br_{0.5})_3$ as a suitable perovskite composition with a bandgap of 1.85 eV (Supplementary Fig. 9). Early studies have shown that for high Br content PSCs with $E_g$ > 1.75 eV, the $V_{oc}$ did not concomitantly increase with $E_g$, which has frequently been attributed to photo-induced halide segregation inside the perovskite active material into bromine- and iodine-rich domains[31]. However, more recently, recombination losses at the interfaces between the wide-gap perovskite and the adjacent charge extraction layers have been found to predominantly limit the $V_{oc}$[8,32]. As such, we aimed to minimize these interfacial losses to achieve the highest possible $V_{oc}$ in our PSCs.

In a first step, we analysed the quasi-Fermi-level splitting (QFLS) in the perovskite on illumination. The QFLS provides an excellent indication (and upper limit) of the $V_{oc}$ that can be expected in an actual solar cell, and it enables us to determine the potential loss in $V_{oc}$ associated with the respective charge extraction layers adjacent to the perovskite. Poly[bis(4-phenyl)(2,4,6-trimethylphenyl)amine] (PTAA) is currently the most prominent HEL in p–i–n PSCs. However, PTAA comes with serious limitations due to the trade-off between efficient hole transport, which requires the PTAA to be as thin as possible, and selectivity, which has been found to impose a lower limit to the PTAA thickness[33]. To overcome the issues associated with PTAA, we use [2-(3,6-dimethoxy-9*H*-carbazol-9-yl)ethyl]phosphonic acid (MeO-2PACz)[13] as the HEL, which forms a dense, pinhole-free self-assembled monolayer on the indium tin oxide (ITO) bottom electrode. In a direct comparison, perovskite layers on MeO-2PACz as the HEL afford a 90 meV larger QFLS compared to their analogues on PTAA (Fig. 2a). Interestingly, in stark contrast to PTAA, with MeO-2PACz as the HEL we also did not observe notable halide segregation under a one-sun-equivalent illumination on a timescale of several minutes, despite using a Br:I ratio of 0.5:0.5 (Supplementary Fig. 10). This is unexpected, as the literature indicates notable halide segregation for Br concentrations in this range[34]. Our findings demonstrate that the proper choice of HEL enables mitigation of halide segregation in perovskites even with elevated Br concentrations. It should be noted that for longer illumination times (>30 min) first indications of reversible halide segregation have been observed (Supplementary Fig. 11), evidencing mitigation, but no complete suppression of halide segregation. A possible origin of the reduced halide segregation with the use of MeO-2PACz as the HEL is discussed in Supplementary Note 2.

Before studying the impact of the electron extraction layer (EEL), we implemented passivation strategies, such as addition of excess lead[35] or modification of the perovskite surface with the organic halide salt phenethylammonium iodide (PEAI)[36,37], which promotes the formation of a two-dimensional (2D) perovskite capping layer (Supplementary Figs. 12–15). As evidenced by photoelectron spectroscopy, the insertion of $PEA^+$ leads to notable lowering of the perovskite valence band maximum (Supplementary Fig. 16), which prevents photogenerated holes from reaching the EEL and thereby improves the selective extraction of electrons.

In the absence of an EEL, the surface passivation does not affect the QFLS (Fig. 2a), which indicates that defects at the surface or grain boundaries do not impose a limit in this scenario. The situation changes if we complete our p–i–n PSCs by adding $PC_{61}BM$ and Al-doped ZnO nanoparticles (AZO NP) as the EEL (Fig. 2b)[38]. Note that for integration of the PSCs in the tandem cell, an additional $SnO_x$ layer, grown by low-temperature atomic layer deposition (ALD), is used, which serves as a permeation barrier and not only improves the long-term stability, but also protects the layers underneath against chemical attack by the solvents of subsequent wet chemical processes[39,40].

By striking contrast to PTAA, with MeO-2PACz as the HEL, the addition of the EEL infers a substantial reduction of the QFLS, and the resulting $V_{oc}$ shows notable further improvements on passivation with excess lead, and even more with the formation of a 2D perovskite cap (Fig. 2c). As the observed mean $V_{oc}$ values reproduce the measured QFLS for devices with MeO-2PACz and the 2D perovskite cap, we conclude that interface recombination, rather than energy misalignment, is the main limiting factor. For champion devices the $V_{oc}$ even reaches the QFLS of the bare perovskite, indicating superior suppression of recombination losses at the EEL interface. Ultimately, PSCs with hysteresis-free current–voltage characteristics are achieved, which provide a very high stabilized $V_{oc}$ = 1.34 V (Fig. 2d, e) with a FF that falls within a narrow range of 77 to 82% (Fig. 2c and Supplementary Fig. 17). In previous reports, an increase of $V_{oc}$ typically came at the cost of a lowered FF and a loss in EQE. A comparison with the literature on high Br content PSCs with an $E_g$ in the range of 1.8–1.9 eV shows that careful mitigation of losses at the interfaces unlocked access to the previously unobtained feature of combined high $V_{oc}$ and FF (Fig. 2e). Finally, when operated continuously

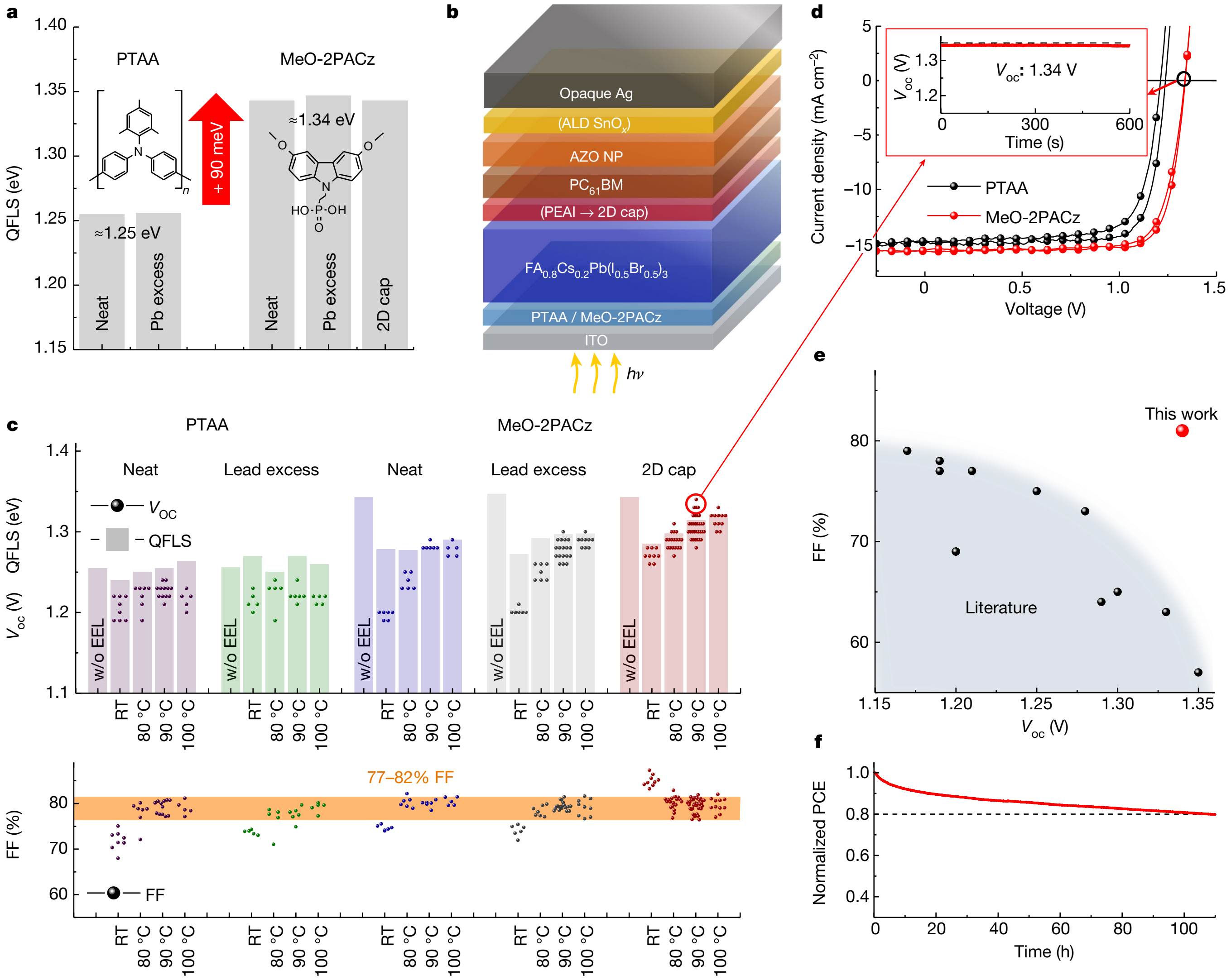

**Fig. 2 | Optimized wide-gap perovskite subcell. a**, Splitting of the quasi Fermi levels (QFLS) in the case of varied HELs, that is, PTAA or MeO-2PACz, with and without use of excessive lead or a 2D capping layer (2D cap, see text). **b**, Layer sequence of the p–i–n perovskite single junction. **c**, Comparison of the open-circuit voltage ($V_{oc}$) of actual PSCs with the corresponding QFLS of representative layer stacks with and without (w/o) EEL and varied device-annealing temperature (RT, room temperature). The FF of each cell type is shown in the lower panel. The different temperatures refer to the annealing conditions after deposition of the AZO NP layer. The dots represent the results of individual devices and indicate the experimental spread. **d**, Current density versus voltage characteristics for champion PSCs with a 2D capping layer (MeO-2PACz self-assembled monolayer (SAM) as the HEL) or $PbI_2$ excess (PTAA as the HEL). The inset shows the stabilized $V_{oc}$ of 1.34 V for the cell with the SAM as the HEL. **e**, Comparison of the $V_{oc}$ and FF of our PSCs with $E_g = 1.85$ eV to PSCs (with $E_g$ in the range of 1.8 to 1.9 eV) with high Br content (≥0.4) reported in the literature. The respective references can be found in Supplementary Table 1. **f**, Normalized PCE versus time of the PSCs illuminated with a white LED and operated in the MPP.

for more than 100 h, the PCE of the wide-gap PSCs remains above 80% of its initial value ($T_{80} = 100$ h) (Fig. 2f).

## Low-loss recombination interconnect

The interconnect is a key component of monolithic (two-terminal) tandem solar cells (Fig. 3a). In a p–i–n tandem, it facilitates the recombination of electrons from the bottom perovskite cell with the holes from the top organic cell, ideally without any loss of $V_{oc}$ and FF. In the simplest approach, one could omit the top electrode of the perovskite cell and stack the organic cell directly on top. In this case, the interface between the low-work-function $SnO_x$ and the high-work-function $MoO_x$ affords only extremely poor, S-shaped *J*–*V* characteristics for the resulting tandem cell (Fig. 3b). This is due to a Schottky barrier of 0.6 eV, which forms at the $SnO_x$/$MoO_x$ interface (Fig. 3c, d and Supplementary Fig. 18).

To render the interconnect ohmic, thin layers (approximately 1 nm) of a metal (Ag or Au) are frequently inserted between the top and bottom cell[10,41]. However, even an Ag layer as thin as 1 nm already introduces notable optical losses, which lower the EQE of the back-cell and the overall $J_{sc}$ of the tandem cell, as is shown further below. Thus, we developed an interconnect based on an ultrathin ALD-grown $InO_x$ layer with a thickness of only about 1.5 nm (details of the ALD growth process can be found in Methods). We leveraged the unique property of ALD to provide utmost control of layer thickness even at the level of ångströms, which is impossible with conventional deposition techniques. The insertion of $InO_x$ between $SnO_x$ and $MoO_x$ outstandingly improves the *J*–*V* characteristics of the tandem cells (Fig. 3b). As few as 32 ALD cycles (thickness approximately 1.5 nm, Supplementary Fig. 19) were sufficient to render the $SnO_x$/$InO_x$/$MoO_x$ stack ohmic (Fig. 3b–d).

To better understand the structural and electronic properties of our interconnect, we conducted high-angle annular dark-field scanning

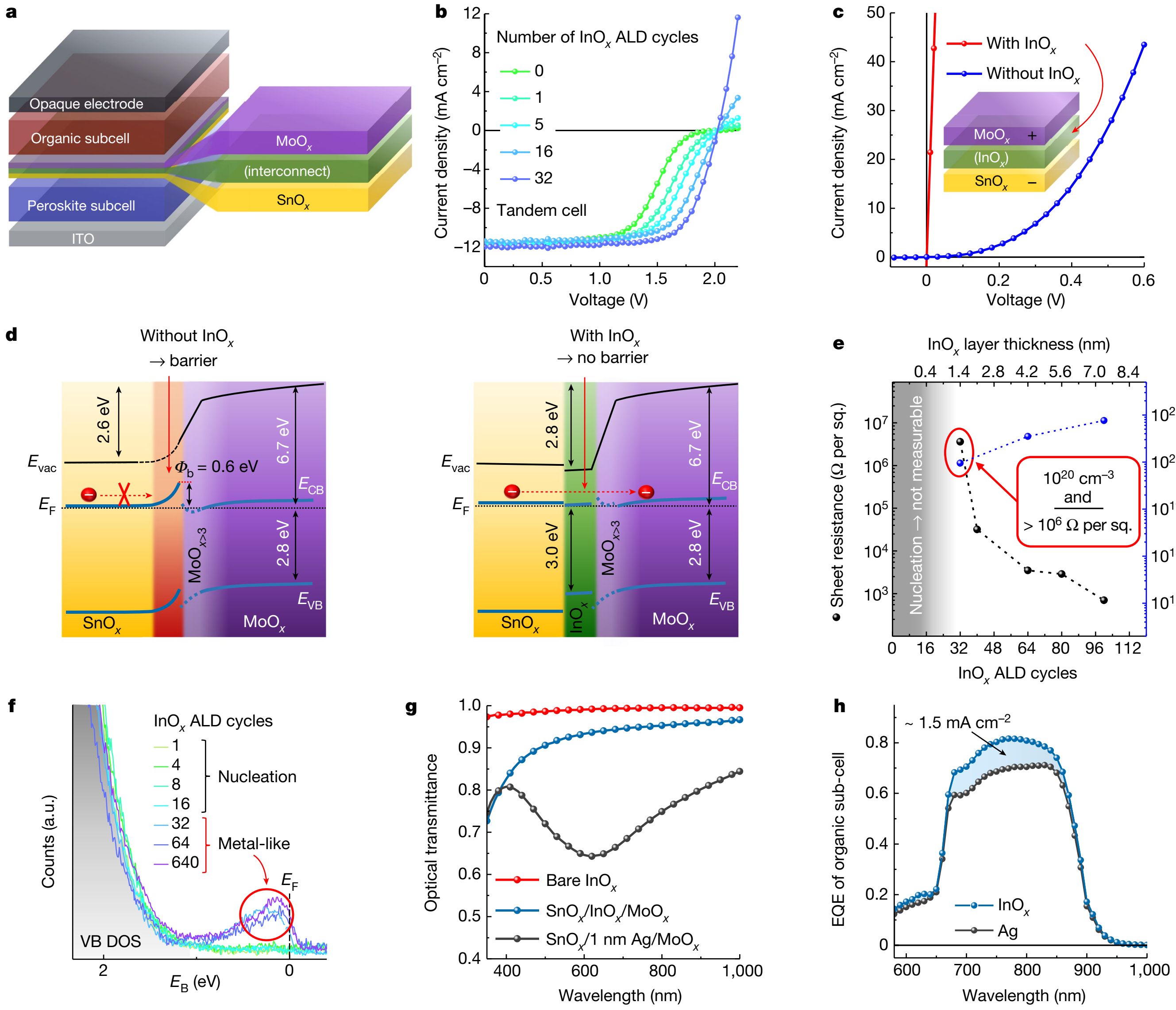

**Fig. 3 | Tandem interconnect.** **a**, Schematic of a perovskite–organic tandem cell with $InO_x$ or Ag as interconnect. **b**, *J*–*V* characteristics of tandem cells with varied thickness (number of ALD cycles) of the $InO_x$ interconnect. **c**, *J*–*V* characteristics of $SnO_x$/($InO_x$)/$MoO_x$ diodes. **d**, Energetic line-up determined with and without $InO_x$. Note, in the first 2 nm of the molybdenum oxide layer we found a mix of oxidation states for the molybdenum, ranging from $Mo^{2+}$ to $Mo^{6+}$ (details in Supplementary Figs. 27–31). The first 2 nm of the molybdenum oxide is characterized by the presence of $MoO_4^{2-}$ clusters (details in Supplementary Information). $E_F$, Fermi level; $E_{vac}$, vacuum level; $E_{CB}$, conduction band; $E_{VB}$, valence band; $\Phi_b$, energy barrier. **e**, Sheet resistance and carrier density versus thickness of the $InO_x$. sq., square. **f**, UPS of the valence band (VB) density of states (DOS) of $InO_x$, showing the onset of a metallic behaviour at 32 cycles of ALD. a.u. arbitrary units. **g**, Optical transmittance of an interconnect based on 32 ALD cycles (approximately 1.5 nm) of $InO_x$, bare and sandwiched between $SnO_x$ and $MoO_x$. For comparison, the $InO_x$ has been replaced by a nominally 1 nm thick layer of Ag. **h**, Resulting EQE spectra of the organic back-cell with $InO_x$ or Ag as interconnect, demonstrating the notable current losses induced by only 1 nm Ag.

transmission electron microscopy (HAADF-STEM), energy dispersive X-ray spectroscopy (EDS), GIWAXS and photoelectron spectroscopy. HAADF-STEM and GIWAXS confirm that our ALD-grown $InO_x$ and $SnO_x$ are both amorphous and continuous (Supplementary Figs. 20–26). Elemental mapping shows that the $SnO_x$/$InO_x$ interface is abrupt, and multivariate analysis[42] confirms no sign of In diffusion into the underlying $SnO_x$ (Supplementary Figs. 22 and 23). As confirmed by highly surface-sensitive ultraviolet (UV) photoelectron spectroscopy (UPS) measurement of the Sn 4*d* semi-core levels, any hypothetical interdiffusion of Sn and In at the $SnO_x$/$InO_x$ interface would be limited to a range of 5 Å (Supplementary Fig. 24). The energetic line-up in the interconnect was unravelled by an extensive study, again using photoelectron spectroscopy (Fig. 3d and Supplementary Figs. 27–31). The upward band bending found in the case of $SnO_x$/$MoO_x$ is completely alleviated by the insertion of the ultrathin $InO_x$, enabling barrier-free transport of electrons from the bottom PSC across the $SnO_x$/$InO_x$/$MoO_x$ layer sequence. Ultimately, these electrons recombine with the holes from the OSC at the $MoO_x$–organic interface[43,44]. Notably, after completion of a nucleation phase (approximately 32 ALD cycles), the $InO_x$ layer shows a metallic nature, with an electron density about $10^{20}$ $cm^{-3}$ (Fig. 3d, e). Although some charge transfer (or doping) at the interface between $SnO_x$ and $InO_x$ cannot be fully excluded, we confirmed that our ALD-grown $InO_x$ also provides a similarly high carrier density when deposited on $Al_2O_3$ (Supplementary Fig. 32). A high carrier density is frequently found in nominally undoped $InO_x$ thin films because of oxygen vacancies and surface defects[45,46]. In our case, we have determined a stoichiometry of $In_2O_{2.8}$ by photoelectron spectroscopy, which indicates oxygen deficiency. As the metallic $InO_x$ layer is ultrathin, it still provides a very high

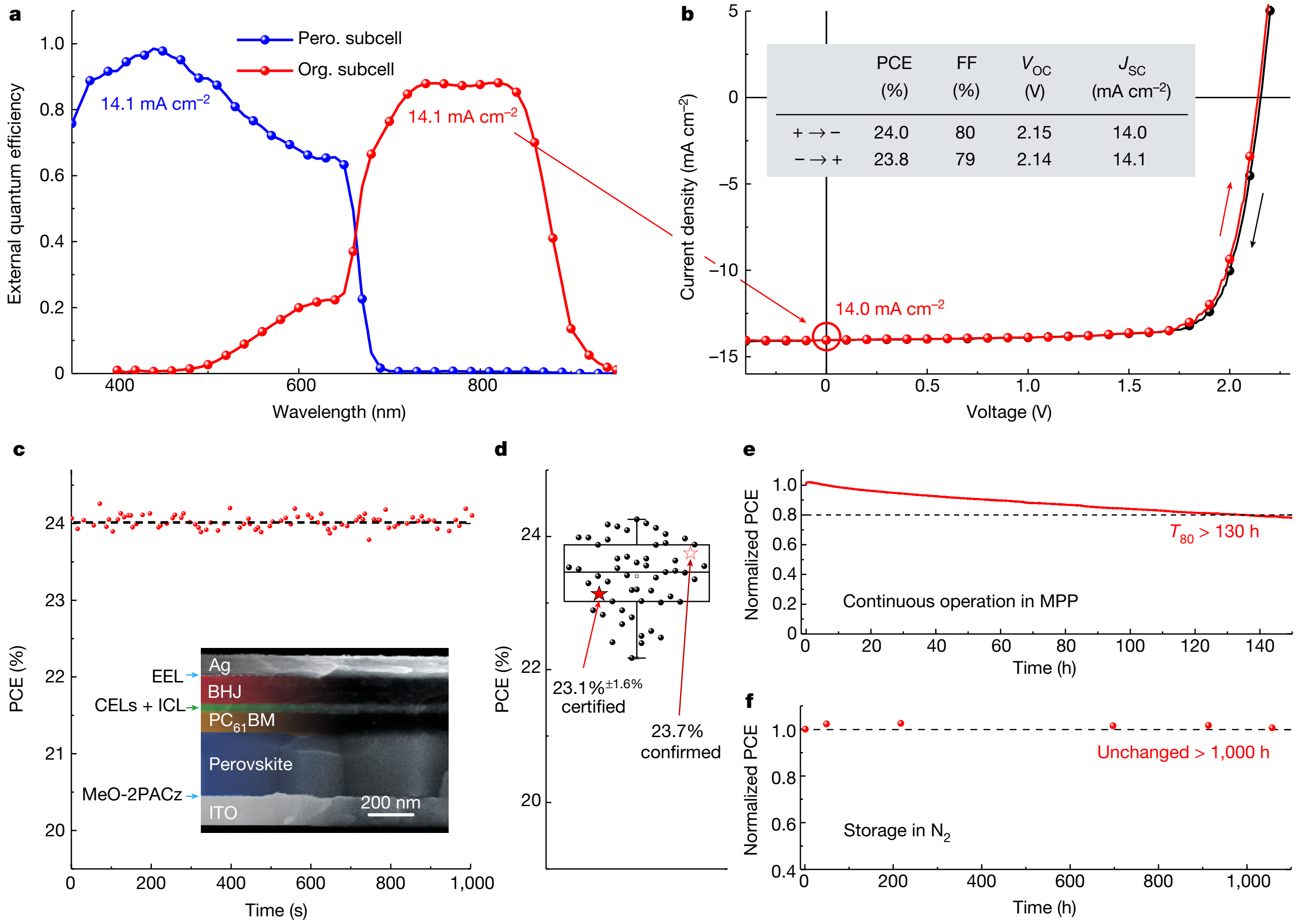

| | PCE (%) | FF (%) | $V_{OC}$ (V) | $J_{SC}$ (mA cm$^{-2}$) |
|---|---|---|---|---|
| + → − | 24.0 | 80 | 2.15 | 14.0 |
| − → + | 23.8 | 79 | 2.14 | 14.1 |

**Fig. 4 | Perovskite–organic tandem cells. a**, EQE spectra of both subcells in the tandem cell. For reduced reflection, the backside of the substrate was coated with a 100 nm thick $MgF_2$ layer. **b**, *J*–*V* characteristics of a tandem cell, with derived PCE, FF, open-circuit voltage ($V_{oc}$) and short-circuit current ($J_{sc}$) shown in the inset. **c**, Stabilized PCE of the tandem cell. Inset: SEM image of the cell cross-section. ICL, interconnecting layer; CELs, charge extraction layers. **d**, Statistical data of 48 tandem solar cells as derived from reverse *J*–*V* scans also containing the certified and confirmed value measured by the Fraunhofer ISE CalLab (Supplementary Figs. 37–39). Median line with upper and lower box ranges denoting the 25% and 75% margins. The bars denote the outermost data points that are still inside another 1.5 interquartile range. **e**, **f**, Stability of the tandem cells under continuous operation in the MPP (**e**) and when stored in $N_2$ (**f**).

sheet resistance of >$10^6$ Ω per square, which outperforms carefully optimized sputtered metal oxide interconnects by at least an order of magnitude[5]. Note that a high sheet resistance is of critical importance to avoid shorting of the subcells in case of local shunt paths.

High carrier densities typically infer optical absorption, which is another important reason to keep the thickness of the interconnect to a minimum[47]. Most strikingly, our ultrathin $InO_x$ interconnect with a transmittance near unity does not introduce notable optical losses (Fig. 3g), which boosts the EQE of the organic back-cell and the overall $J_{sc}$ of the tandem by about 1.5 mA cm$^{-2}$ compared to the case of an interconnect based on 1 nm of Ag, which affords a PCE of only about 20% (Fig. 3h and Supplementary Fig. 33). ALD enables large-area, high-throughput processing (even at atmospheric pressure)[48], and also enables conformal coating of textured surfaces that frequently occur in light-trapping concepts[2]. Hence, we predict that the applicability of our interconnect is not limited to perovskite–organic tandem cells, and it may also be favourably used in other tandem cells.

## Perovskite–organic tandem cells

Drawing from the progress outlined above, we prepared monolithic perovskite–organic tandem solar cells with outstanding characteristics. The EQE spectra of the PSC and OSC subcells of an optimized perovskite–organic tandem are shown in Fig. 4a. Excellent current matching, as is required in a series connection, is evidenced by the identical integrated current density of 14.1 mA cm$^{-2}$ for both subcells. The high EQE values (>95%) in the wavelength region between 400 and 500 nm can be explained by optical effects associated with the high refractive index of the perovskite material, which affords an efficient in-coupling of light into the active medium in this spectral range[49]. The high $V_{oc}$ = 2.15 V of the tandem cell results from an almost ideal addition of the *J*–*V* characteristics of the subcells without any loss in $V_{oc}$ (Table 1, Fig. 4b and Supplementary Fig. 34). As a result, a champion tandem cell with a stabilized PCE of 24.0% is achieved (Fig. 4b, c and Supplementary Figs. 35 and 36). An efficiency of 23.1% (±1.6%) was certified by the Fraunhofer ISE CalLab, according to the IEC 60904-3 procedure (Fig. 4d and Supplementary Figs. 37–39). As the certification procedure inflicts some stress to the device before the actual certification (Supplementary Note 4), an additional control measurement (without certificate) was conducted by the Fraunhofer ISE CalLab without the stressing conditions, which confirmed an efficiency of 23.7%, as we had measured in our laboratory (Supplementary Fig. 40).

Our devices are shown to be the most efficient monolithic perovskite–organic tandem cells achieved so far. The tandem characteristics show a very small statistical variation (Supplementary Figs. 35 and 36), resulting from robust processing of the perovskite subcell[50]. We show an excellent stability of more than 1,000 h with no sign of degradation when the devices are kept under inert atmosphere, and a $T_{80}$ of 130 h under continuous operation in the MPP (Fig. 4e, f). Note that the temporal behaviour of the tandem under continuous operation is essentially governed by that of the perovskite subcell (Fig. 2f).

## Online content

Any methods, additional references, Nature Research reporting summaries, source data, extended data, supplementary information, acknowledgements, peer review information; details of author contributions and competing interests; and statements of data and code availability are available at https://doi.org/10.1038/s41586-022-04455-0.

1. Leijtens, T., Bush, K. A., Prasanna, R. & McGehee, M. D. Opportunities and challenges for tandem solar cells using metal halide perovskite semiconductors. *Nat. Energy* **3**, 828–838 (2018).
2. Hou, Y. et al. Efficient tandem solar cells with solution-processed perovskite on textured crystalline silicon. *Science* **367**, 1135–1140 (2020).
3. Han, Q. et al. High-performance perovskite/Cu(In,Ga)Se$_2$ monolithic tandem solar cells. *Science* **361**, 904–908 (2018).
4. Lin, R. et al. Monolithic all-perovskite tandem solar cells with 24.8% efficiency exploiting comproportionation to suppress Sn(II) oxidation in precursor ink. *Nat. Energy* **4**, 864–873 (2019).
5. Palmstrom, A. F. et al. Enabling flexible all-perovskite tandem solar cells. *Joule* **3**, 2193–2204 (2019).
6. Yan, C. et al. Non-fullerene acceptors for organic solar cells. *Nat. Rev. Mater.* **3**, 18003 (2018).
7. Liu, Q. et al. 18% Efficiency organic solar cells. *Sci. Bull.* **65**, 272–275 (2020).
8. Mahesh, S. et al. Revealing the origin of voltage loss in mixed-halide perovskite solar cells. *Energy Environ. Sci.* **13**, 258–267 (2020).
9. Li, C., Wang, Y. & Choy, W. C. H. Efficient interconnection in perovskite tandem solar cells. *Small Methods* **4**, 2000093 (2020).
10. Chen, X. et al. Efficient and reproducible monolithic perovskite/organic tandem solar cells with low-loss interconnecting layers. *Joule* **4**, 1594–1606 (2020).
11. Zhan, L. et al. Over 17% efficiency ternary organic solar cells enabled by two non-fullerene acceptors working in an alloy-like model. *Energy Environ. Sci.* **13**, 635–645 (2020).
12. Degani, M. et al. 23.7% Efficient inverted perovskite solar cells by dual interfacial modification. *Sci. Adv.* **7**, 7930 (2021).
13. Al-Ashouri, A. et al. Conformal monolayer contacts with lossless interfaces for perovskite single junction and monolithic tandem solar cells. *Energy Environ. Sci.* **12**, 3356–3369 (2019).
14. Shockley, W. & Queisser, H. J. Detailed balance limit of efficiency of p–n junction solar cells. *J. Appl. Phys.* **32**, 510–519 (1961).
15. Graetzel, M. The light and shade of perovskite solar cells. *Nat. Mater.* **13**, 838–842 (2014).
16. McMeekin, D. P. et al. A mixed-cation lead mixed-halide perovskite absorber for tandem solar cells. *Science* **351**, 151–155 (2016).
17. Tao, S. et al. Absolute energy level positions in tin- and lead-based halide perovskites. *Nat. Commun.* **10**, 2560 (2019).
18. Hao, F., Stoumpos, C. C., Chang, R. P. H. & Kanatzidis, M. G. Anomalous band gap behavior in mixed Sn and Pb perovskites enables broadening of absorption spectrum in solar cells. *J. Am. Chem. Soc.* **136**, 8094–8099 (2014).
19. Zhao, D. et al. Efficient two-terminal all-perovskite tandem solar cells enabled by high-quality low-bandgap absorber layers. *Nat. Energy* **3**, 1093–1100 (2018).
20. Green, M. A. et al. Solar cell efficiency tables (version 56). *Prog. Photovolt. Res. Appl.* **28**, 629–638 (2020).
21. Yu, G., Gao, J., Hummelen, J. C., Wudl, F. & Heeger, A. J. Polymer photovoltaic cells: enhanced efficiencies via a network of internal donor-acceptor heterojunctions. *Science* **270**, 1789–1791 (1995).
22. Zhao, J. et al. Efficient organic solar cells processed from hydrocarbon solvents. *Nat. Energy* **1**, 15027 (2016).
23. Cheng, P., Li, G., Zhan, X. & Yang, Y. Next-generation organic photovoltaics based on non-fullerene acceptors. *Nat. Photon.* **12**, 131–142 (2018).
24. Qian, D. et al. Design rules for minimizing voltage losses in high-efficiency organic solar cells. *Nat. Mater.* **17**, 703–709 (2018).
25. Liu, J. et al. Fast charge separation in a non-fullerene organic solar cell with a small driving force. *Nat. Energy* **1**, 16089 (2016).
26. Yuan, J. et al. Single-junction organic solar cell with over 15% efficiency using fused-ring acceptor with electron-deficient core. *Joule* **3**, 1140–1151 (2019).
27. Yu, R. et al. Improved charge transport and reduced nonradiative energy loss enable over 16% efficiency in ternary polymer solar cells. *Adv. Mater.* **31**, 1902302 (2019).
28. Zhu, Y. et al. Rational strategy to stabilize an unstable high-efficiency binary nonfullerene organic solar cells with a third component. *Adv. Energy Mater.* **9**, 1900376 (2019).
29. Gasparini, N. et al. Exploiting ternary blends for improved photostability in high-efficiency organic solar cells. *ACS Energy Lett.* **5**, 1371–1379 (2020).
30. Du, X. et al. Unraveling the microstructure-related device stability for polymer solar cells based on nonfullerene small-molecular acceptors. *Adv. Mater.* **32**, 1908305 (2020).
31. Slotcavage, D. J., Karunadasa, H. I. & McGehee, M. D. Light-induced phase segregation in halide-perovskite absorbers. *ACS Energy Lett.* **1**, 1199–1205 (2016).
32. Peña-Camargo, F. et al. Halide segregation versus interfacial recombination in bromide-rich wide-gap perovskite solar cells. *ACS Energy Lett.* **5**, 2728–2736 (2020).
33. Stolterfoht, M. et al. Approaching the fill factor Shockley–Queisser limit in stable, dopant-free triple cation perovskite solar cells. *Energy Environ. Sci.* **10**, 1530–1539 (2017).
34. Knight, A. J. & Herz, L. M. Preventing phase segregation in mixed-halide perovskites: a perspective. *Energy Environ. Sci.* **13**, 2024–2046 (2020).
35. Park, B.-W. et al. Understanding how excess lead iodide precursor improves halide perovskite solar cell performance. *Nat. Commun.* **9**, 3301 (2018).
36. Jiang, Q. et al. Surface passivation of perovskite film for efficient solar cells. *Nat. Photon.* **13**, 460–466 (2019).
37. Doung, T. et al. High efficiency perovskite-silicon tandem solar cells: effect of surface coating versus bulk incorporation of 2D perovskite. *Adv. Energy Mater.* **10**, 1903553 (2020).
38. Brinkmann, K. O. et al. Suppressed decomposition of organometal halide perovskites by impermeable electron-extraction layers in inverted solar cells. *Nat. Commun.* **8**, 13938 (2017).
39. Behrendt, A. et al. Highly robust transparent and conductive gas diffusion barriers based on tin oxide. *Adv. Mater.* **27**, 5961–5967 (2015).
40. Gahlmann, T. et al. Impermeable charge transport layers enable aqueous processing on top of perovskite solar cells. *Adv. Energy Mater.* **10**, 1903897 (2020).
41. Gu, S. et al. Tin and mixed lead–tin halide perovskite solar cells: progress and their application in tandem solar cells. *Adv. Mater.* **32**, 1907392 (2020).
42. Zhang, S. & Scheu, C. Evaluation of EELS spectrum imaging data by spectral components and factors from multivariate analysis. *Microscopy* **67**, 133–141 (2018).
43. Becker, T. et al. All-oxide MoO$_x$/SnO$_x$ charge recombination interconnects for inverted organic tandem solar cells. *Adv. Energy Mater.* **8**, 1702533 (2018).
44. Meyer, J. et al. Transition metal oxides for organic electronics: energetics, device physics and applications. *Adv. Mater.* **24**, 5408–5427 (2012).
45. Hagleitner, D. R. et al. Bulk and surface characterization of In$_2$O$_3$(001) single crystals. *Phys. Rev. B* **85**, 115441 (2012).
46. Lany, A. et al. Surface origin of high conductivities in undoped In$_2$O$_3$ thin films. *Phys. Rev. Lett.* **108**, 016802 (2012).
47. Bellingham, J. R., Phillips, W. A. & Adkins, C. J. Intrinsic performance limits in transparent conducting oxides. *J. Mater. Sci. Lett.* **11**, 263–265 (1992).
48. Hoffmann, L. et al. Spatial atmospheric pressure atomic layer deposition of tin oxide as an impermeable electron extraction layer for perovskite solar cells with enhanced thermal stability. *ACS Appl. Mater. Interfaces* **10**, 6006–6013 (2018).
49. Brinkmann, K. O. et al. The optical origin of near-unity external quantum efficiencies in perovskite solar cells. *Sol. RRL* **9**, 2100371 (2021).
50. Brinkmann, K. O. et al. Extremely robust gas-quenching deposition of halide perovskites on top of hydrophobic hole transport materials for inverted (p–i–n) solar cells by targeting the precursor wetting issue. *ACS Appl. Mater. Interfaces* **11**, 40172–40179 (2019).

# Methods

## Materials synthesis and device preparation

**Perovskite subcell and interconnect.** All processing steps of each subcell were carried out either in an inert atmosphere or under high vacuum without inert breaks.

The layer sequence of the perovskite p–i–n subcell is glass/HEL/$FA_{0.8}Cs_{0.2}Pb(I_{0.5}Br_{0.5})_3$/$PC_{61}BM$/AZO-NP/ALD-$SnO_x$/ALD-$InO_x$/(Ag). As substrate we used ITO-coated glass (17 × 17 mm$^2$) with a photoresist patterned to define the active area of 3.14 mm$^2$. Tandem cells, additionally, were covered with an illumination mask reducing the active area to 1.74 mm$^2$ to match the certification procedure. After cleaning and a brief plasma treatment, PTAA (Sigma-Aldrich, 1.35 mg ml$^{-1}$ in toluene) or MeO-2PACz (TCI, 0.1 mM in ethanol) was spin-coated at 6,000 r.p.m. for 20 s with a ramp of 8 s and annealed at 100 °C for 30 min. For perovskite thin-film preparation, $PbI_2$ (0.75 M, ultra-dry from Alfa Aesar), $PbBr_2$ (0.25 M, ultra-dry from Alfa Aesar), CsBr (0.2 M, ultra-dry from Alfa Aesar) and FABr (0.8 M, from Greatcell Solar) were dissolved in a 3:7 mixture of *N*-methyl-pyrrolidone and dimethylformamide and stirred for at least 3 h. In some cases, an additional 20 mM $PbI_2$ and 10 mM $PbBr_2$ were added. Before spin-coating, 33 mM thiourea (2.5 mg ml$^{-1}$, Sigma-Aldrich; previously dissolved as 100 mg ml$^{-1}$ in dimethylformamide) was added to the precursor solution. The perovskite deposition was performed following a gas-quenching procedure, as described in earlier work[50]. Briefly, the solution was spin-coated at 3,000 r.p.m. for 120 s with a ramp of 10 s. About 15 s after the ramp was finished, a nitrogen flow (7 bar, filtered with 5.0 µm PTFE) was directed at the substrate to introduce a supersaturated intermediate phase. Subsequently, during a 20 min annealing step at 100 °C, the final perovskite layer formed. PEAI (TCI, 1 mg ml$^{-1}$ in isopropanol) was optionally spin-coated at 6,000 r.p.m. for 30 s with a ramp of 8 s followed by another annealing step of 10 min at 100 °C. The optimum $PC_{61}BM$ layer thickness (Supplementary Fig. 41) was found to be around 100 nm for the following process parameters: $PC_{61}BM$ purchased from Ossila, 50 mg ml$^{-1}$ in chlorobenzene, was spin-coated with 1,000 r.p.m. for 30 s and a ramp of 1 s. AZO nanoparticles were processed from an NP-dispersion (Avantama AG, N21x, 2.5 wt% in a mixture of alcohols) diluted with isopropanol (1:2) and spin-coated at 4,000 r.p.m. for 20 s using a ramp of 6 s. Some AZO layers were subsequently annealed at 80 °C, 90 °C or 100 °C for 90 min. For ALD deposition the solar cells were transferred into a Beneq TFS-200 reactor without inert break. $SnO_x$ layers were grown from tetrakis(dimethylamino)tin(IV) (TDMA-Sn, Strem) and water. The reactor temperature during the deposition was 80 °C, TDMA-Sn was kept in a hot source at 45 °C and water in a liquid source at room temperature. Directly thereafter, $InO_x$ was grown on top of $SnO_x$ from cyclopentadienylindium (CpIn, Strem), oxygen (purity 99.999%) and water[51]. The reactor temperature was 80 °C, CpIn was kept in a hot source at 50 °C and water was kept in a liquid source at room temperature.

Note that although our ALD processes are based on water as the oxygen source, which one might intuitively suspect to be detrimental to the active perovskite material, a single dose of $H_2O$ in low-pressure ALD typically creates an environment equivalent to a maximum of 0.1% relative humidity[52]. This is substantially lower than the large variety of conditions mentioned in the literature to degrade perovskite[53,54].

Silver was thermally evaporated in high vacuum ($10^{-7}$ mbar).

**Preparation of the organic subcell.** As hole extractor, a 15 nm layer of $MoO_x$ was thermally evaporated in high vacuum ($10^{-7}$ mbar). To form the binary bulk heterojunction (BHJ) PM6 and Y6 (Solarmer Materials) with a weight ratio of 1:1.2 were dissolved in chloroform (polymer concentration 7 mg ml$^{-1}$) and stirred for 3 h at 50 °C. For the ternary BHJ an extra amount of $PC_{61}BM$ (American Dye Source) was added, yielding a weight ratio of 1:1.2:0.2. Five minutes before BHJ processing 0.5 vol% of 1-chloronaphthalene (Sigma-Aldrich) was added to the solution. Spin-coating was carried out dynamically (solution was dropped onto the middle of the rotating substrate) at 2,500 r.p.m. for 60 s. A subsequent thermal annealing step at 100 °C was applied followed by thermal evaporation of 10 nm $C_{60}$, 5 nm of BCP and 100 nm Ag.

For selected tandem cells, a 100 nm thick $MgF_2$ layer was thermally evaporated onto the back side of the glass substrate as an antireflection layer.

## Materials and device characterization

***J*–*V* and stabilized power output.** *J*–*V* characteristics of solar cells were recorded outside the glovebox under a continuous flow of nitrogen using a Keithley 2400 source measurement unit (SMU) and a 300 W Newport solar simulator (model 91160, AM1.5G, 100 mW cm$^{-2}$) calibrated with a certified IEC 60904-9-compliant Si reference cell (Rera Systems). *J*–*V* characteristics were recorded with a scanning speed of 500 mV s$^{-1}$. Stabilized power output recording was performed by continuously tracking the MPP under AM1.5G illumination. Stabilized $V_{oc}$ was recorded by continuously recording voltage without current flow. Long-term measurements were conducted by continuous MPP tracking in an $N_2$-purged chamber under the illumination of two high-power LED light sources (NIR: Thorlabs M850LP1, and visible: Prizmatics UHP-T-HCRI or Thorlabs MWWHLP1 with a 630 nm low-pass filter) joined together by a dichroic mirror. We set the intensity of the light source(s) to generate a $J_{sc}$ comparable to AM1.5G sunlight illumination, unless otherwise stated. In the case of organic single junctions, this was achieved by first tuning the intensity of the $LED_{NIR}$ to match the $J_{sc}$ to that of the tandem under AM1.5G illumination. Then the white $LED_{VIS}$ was added to finally achieve a $J_{sc}$ corresponding to that of the organic single junctions under AM1.5G illumination. For the perovskite single junctions only the white $LED_{VIS}$ was used for illumination.

Temperature-dependent *J*–*V* scans of the recombination layers were conducted with an all-in-one solar cell characterization system (PAIOS, Fluxim) connected to a temperature-controlled cryostat (Linkham). Temperature was varied from room temperature upwards, then down and back to room temperature to ensure reproducibility.

**EQE characterization.** For EQE measurements a home-built set-up containing a chopped tunable light source (LOT MSH150) and a lock-in amplifier (NF Electronic Instruments 5610B) was used. Calibration was performed with a Thorlabs PM100D power meter with a S130VC sensor head. For determination of the EQE of the tandem cells a previously published protocol was followed[55]. The subcells were therefore characterized under accurate bias conditions, to emulate operation under AM1.5G illumination. A 780 nm and a 520 nm laser diode (RLDC780-2-3 and RLCW520F, Roithner LaserTechnik) were used as bias light sources for the narrow-gap and wide-gap subcells, respectively.

**Electrical characterization of thin films.** Sheet resistance was determined by measurements following the van der Pauw geometry in a home-built set-up using a Keithley 2400 SMU and Keithley 182 voltmeter. Charge carrier density was determined from Hall measurements using the same set-up and a magnetic field of 0.75 T.

**Photoelectron spectroscopy.** Photoelectron spectroscopy was performed in a custom-built ultra-high vacuum system, with a base pressure <$10^{-9}$ mbar. For the detection of the photoelectrons in the UPS and X-ray photoelectron spectroscopy (XPS) measurements, a hemispherical energy analyser was used (Specs Phoibos 100). The excitation for XPS was done via a non-monochromated $MgK_\alpha$ source (from VG Scienta, $h\nu$ = 1,253.6 eV) and for UPS by a monochromatic He source (VUV500, VG Scienta, $h\nu$ = 21.22 eV). Inverse photoemission spectroscopy (IPES) was performed using a Kimball electron source (ELG-2) and a solid-state band-pass filter (Omnivac IPES2000). The samples were transferred into the measurement system without air exposure and were measured within 2 days of preparation.

The program XPSPEAK v.4.1. was used to fit the XPS spectra. For fitting of the molybdenum XPS peaks, a Shirley background was subtracted. The parameter for full width half maximum and the Lorentzian to Gaussian ratio (L:G) were kept constant for all Mo peaks, at 1.22 eV and 23, respectively. The distances between the peaks of the different Mo oxidation states were held constant, with 0.82 eV between $Mo^{5+}$ and $Mo^{6+}$ and 0.8 eV between $Mo^{4+}$ and $Mo^{5+}$. With regard to the additional Mo feature that we observed (Supplementary Fig. 28): in the case of $MoO_x$ on top of $SnO_x$, the position was at 0.88 eV higher binding energy compared to the $Mo^{6+}$ signal of $MoO_x$, whereas on $InO_x$ this shift was 0.74 eV.

**X-ray diffraction and scattering.** X-ray diffraction characterization was conducted with a $CuK_{\alpha 1,2}$ source (Philips C’Pert Pro MPD).

GIWAXS and GISAXS were performed on a Xenocs XEUSS 2.0 laboratory beamline using $CuK_\alpha$ radiation. Sample detector distances were 170 mm and 1,470 mm for GIWAXS and GISAXS, respectively. The incident angles were below 0.5°, and the pressure in the sample chamber during the experiment was 0.1 bar. X-ray reflectivity measurements were recorded with a GE XRD 3003 TT diffractometer in ambient environment, also using $CuK_\alpha$ radiation. Synchrotron GIWAXS measurements were done at beamline ID10 of the ESRF under nitrogen conditions. Beam energy was 22 keV, with incidence angles varying from 0 to 0.3°.

**Atomic force microscopy, electron microscopy and spectroscopy.** Scanning electron microscopy (SEM) images were obtained with a Phillips XL-30 SFEG. AFM was conducted with a Bruker Innova system.

Scanning transmission electron microscopy (STEM) was performed on a Titan Themis microscope operated at 300 kV. The aberration-corrected STEM probe had a <1 Å size and a convergence semi-angle of 24 mrad. High-angle annular dark-field (HAADF) and annular bright-field images were acquired using collection angles of 73–200 and 8–16 mrad, respectively. The cross-sectional sample for STEM was prepared by a Scios2 focused-ion beam (FIB) with a C marker layer to protect the sample surface[56].

Energy-dipsersive spectroscopy (EDS) spectral imaging was collected by a SuperX detector. The elemental distribution within the ALD layers was examined by EDS spectrum imaging, as shown in Supplementary Fig. 22. It is noteworthy that the In L and Sn L X-ray emission peaks overlap, so that the traditional quantification by integrating peak intensity over fixed windows leads to interference between the $SnO_x/InO_x$ layers. Therefore, we applied multivariate statistical analysis to separate the X-ray emission signals from In and Sn. In this case, we used non-negative matrix factorization, an algorithm widely applied in microanalysis, including spectrum imaging of EDS and electron energy loss spectroscopy[42,57].

**Optical characterization.** Ellipsometry data for the metal oxide layers were acquired with a J.A. Woollam M-2000V ellipsometer and fitted with a Cauchy approximation. Optical simulations were carried out using SETFOS (Fluxim). Details of the simulation can be found in Supplementary Note 2. Transmittance spectra were obtained using the same tunable light source as used for EQE (not chopped) and a power meter. The respective layers were deposited on quartz substrates. UV–visible spectra were acquired with a Jasco V-670 spectrometer. LED spectra were determined using an Ocean Optics spectrometer (USB2000+XR1-ES).

Excitation for the photoluminescence imaging measurements was performed with a 520 nm CW laser (Insaneware) through an optical fibre into an integrating sphere. The intensity of the 1 cm² laser spot was adjusted to a 1 Sun equivalent intensity by illuminating a wide-gap perovskite solar cell under short circuit and matching the current density to the $J_{sc}$ under the sun simulator (for example, approximately 16 mA cm$^{-2}$ at 100 mW cm$^{-2}$, or $1 \times 10^{21}$ photons per m² per s for a perovskite cell with a bandgap of 1.85 eV). A second optical fibre was used from the output of the integrating sphere to an Andor SR393i-B spectrometer equipped with a silicon CCD camera (DU420A-BR-DD, iDus). The system was calibrated by using a halogen lamp with known spectral irradiance, which was shone into the integrating sphere. A spectral correction factor was established to match the spectral output of the detector to the calibrated spectral irradiance of the lamp. The spectral photon density was obtained from the corrected detector signal (spectral irradiance) by division through the photon energy, and the photon numbers of the excitation and emission were obtained from numerical integration using Matlab. In a last step, three fluorescent test samples with high specified photoluminescence quantum yield (PLQY) (approximately 70%) supplied from Hamamatsu Photonics were measured, where the specified value could be accurately reproduced within a small relative error of less than 5%.

**Quantification of the QFLS in partial cell stacks.** To calculate the QFLS, we can use the Shockley–Queisser equation, which links the radiative recombination density of free charges ($J_{rad}$) with the chemical potential per free electron–hole pair ($\mu$) or the QFLS in the active material[14,58].

$$J_{rad} = J_{0,rad} \exp(\mu / k_B T) \tag{1}$$

Here $J_{0,rad}$ is the radiative thermal recombination current density in the dark, $k_B$ the Boltzmann constant and $T$ the temperature. We note that equation (1) is a simplification of Würfel's generalized Planck law, which is only valid for a QFLS that is a few $k_BT$ smaller that the bandgap $\mu < E_G - 3k_BT$ (ref. [59]). If radiative recombination comes only from free charges, the radiative recombination current is identical to the photoluminescene yield times the elementary charge, that is, $J_{rad} = \Phi_{PL} \times q$. Moreover, we can define the PLQY as the ratio of radiative to total recombination ($J_{R,tot}$), where the latter is identical to the generation current density ($J_G$) under open-circuit conditions ($V_{oc}$)

$$\mathrm{PLQY} = J_{rad}/J_{R,tot} = J_{rad}/J_G \tag{2}$$

Therefore, we can relate the QFLS to the measured PLQY in the following way

$$\mu = k_B T \ln(\mathrm{PLQY} \times J_G / J_{0,rad}) \tag{3}$$

We also note that equations (2) and (3) are only valid if the spectral dependence of $J_{rad}$ is identical to $J_{0,rad}$, meaning recombination goes through the same channels regardless of the QFLS.

To quantify the intensity dependence of the QFLS, we consider the following points. First, equation (3) shows that the QFLS depends on the temperature. We note that we have measured the temperature on the samples during the illumination at various light intensities using an infrared sensor. Even at an intensity of 5 equivalent suns, which is the upper limit for the results shown in the main text, we observe a negligible temperature increase on the sample (≈1 °C). We attribute this to the fast dissipation of heat from the rather small illumination spot area (1 cm²) during the measurement.

Second, the generation current density $J_G$ was approximated with the short-circuit current density of the complete solar cell. Similarly, the $J_{0,rad}$ was estimated by integrating the overlap of the EQE of the device with the black-body spectrum $\Phi_{BB}$ at 300 K over the energy.

$$J_{0,rad} = \int \mathrm{EQE} \times \Phi_{BB} \, d\epsilon \tag{4}$$

## Data availability

The data that support the findings of this study are available from the corresponding authors upon reasonable request.

51. Libera, J. A., Hryn, J. N. & Elam, J. W. Indium oxide atomic layer deposition facilitated by the synergy between oxygen and water. *Chem. Mater.* **23**, 2150–2158 (2011).
52. Zardetto, V. et al. Atomic layer deposition for perovskite solar cells: research status, opportunities and challenges. *Sustain. Energy Fuels* **1**, 30–55 (2017).
53. Wei, W. & Hu, Y. W. Catalytic role of $H_2O$ in degradation of inorganic–organic perovskite ($CH_3NH_3PbI_3$) in air. *Int. J. Energy Res.* **41**, 1063–1069 (2017).
54. Yang, J., Siempelkamp, B. D., Liu, D. & Kelly, L. D. Investigation of $CH_3NH_3PbI_3$ degradation rates and mechanisms in controlled humidity environments using in situ techniques. *ACS Nano* **9**, 1955–1963 (2015).
55. Timmreck, R. et al. Characterization of tandem organic solar cells. *Nat. Photon.* **9**, 478–479 (2015).
56. Zhang, S. et al. Different photostability of $BiVO_4$ in near-pH-neutral electrolytes. *ACS Appl. Energy Mater.* **3**, 9523–9527 (2020).
57. Shiga, M. et al. Sparse modeling of EELS and EDX spectral imaging data by nonnegative matrix factorization. *Ultramicroscopy* **170**, 43–59 (2016).
58. Wurfel, P. The chemical potential of radiation. *J. Phys. C* **15**, 3967–3985 (1982).
59. Würfel P. & Würfel U. Physics of Solar Cells: From Basic Principles to Advanced Concepts (Wiley, 2016).

**Acknowledgements** We acknowledge the Deutsche Forschungsgemeinschaft (DFG) (within the SPP 2196: grant numbers RI 1551/15-1, RI 1551/12-1; individual grant numbers: RI 1551/18-1, RI 1551/4-3, RI 1551/7-2 and HE 2698/7-2), the Bundesministerium für Bildung und Forschung (BMBF) (grant number: 01DP20008) and the Bundesministerium für Wirtschaft und Energie (BMWi) (grant number: ZF4037809DF8) for financial support. The research leading to these results has received partial funding from the European Union's Horizon 2020 Programme under grant agreement no. 951774 (FOXES). This work was also partially funded by the European Regional Development Fund (ERDF) (grant number: EFRE 0801507), S.O. and C. Koch further thank the SCALUP project. (SOLAR-ERA.NET Cofund 2, id: 32). We thank Mountain Photonics for providing us with a Prizmatix high-power white LED as well as Tesa Germany for providing us with sealing duct tape. We also thank J. Wang and R. Janssen from the Eindhoven University of Technology for their support in verifying some EQE values reported in this work. We thank B. Gault and A. Sturm from the Max-Planck-Institut für Eisenforschung GmbH for help with the FIB and for enabling the STEM measurements. We also thank the ESRF for the admission of X-ray diffraction measurements and gratefully appreciate the support by our local contacts O. Konovalov and M. Jankowski. Finally, we acknowledge J. Hohl-Ebinger from the Fraunhofer ISE CalLab for valuable consultation throughout the certification process.

**Author contributions** T.R., T.B. and K.O.B. conceived and designed the experiments. S.O. and C. Koch contributed the XPS, UPS and IPES analysis. K.O.B., T.B., F.Z., C. Kreusel, M.G., T.M., C.T. and F.G. performed the experimental work on the solar cells. T.G. and M.T. contributed the metal oxide ALD layers as well as electrical characterization. T.H. did the cross-section SEM measurements. P.C., L.P.-T., D.N. and M.S. designed, conducted and evaluated the PLQY/QFLS studies. A.A.-A. and S.A. provided the expertise in the processing of the self-assembled monolayers. D.H. and K.M. contributed temperature-dependent *J*–*V* characterization. L.M., A.H. and F.S. designed and conducted the GIWAXS and L.G. and S.Z. the HAADF-STEM and EDS studies. All authors discussed the results and were involved in the writing.

**Competing interests** The authors declare no competing interests.

**Additional information**

**Supplementary information** The online version contains supplementary material available at https://doi.org/10.1038/s41586-022-04455-0.

**Correspondence and requests for materials** should be addressed to K. O. Brinkmann or T. Riedl.

**Peer review information** *Nature* thanks the anonymous reviewers for their contribution to the peer review of this work.